Impact of Synoptic Atmospheric Forcing on the Mean Ocean Circulation

Yang Wu[1, 2], Xiaoming Zhai[3*], and Zhaomin Wang[1, 2]

[1]*Polar Climate System and Global Change Laboratory, Nanjing University of Information Science and Technology, Nanjing, China*

[2]*Earth System Modelling Center, Nanjing International Academy of Meteorological Sciences, Nanjing University of Information Science and Technology, Nanjing, China*

[3]*Centre for Ocean and Atmospheric Sciences, School of Environmental Sciences, University of East Anglia, Norwich, United Kingdom*

**Corresponding author address:* Xiaoming Zhai, School of Environmental Sciences, University of East Anglia, Norwich NR4 7TJ, United Kingdom. E-mail: Xiaoming.Zhai@uea.ac.uk

ABSTRACT

The impact of synoptic atmospheric forcing on the mean ocean circulation is investigated by comparing simulations of a global eddy-permitting ocean-sea ice model forced with and without synoptic atmospheric phenomena. Consistent with previous studies, transient atmospheric motions such as weather systems are found to contribute significantly to the time-mean wind stress and surface heat loss at mid and high latitudes owing to the nonlinear nature of air-sea turbulent fluxes. Including synoptic atmospheric forcing in the model has led to a number of significant changes. For example, wind power input to the ocean increases by about 50%, which subsequently leads to a similar percentage increase in global eddy kinetic energy. The wind-driven subtropical gyre circulations are strengthened by about 10-15%, whereas even greater increases in gyre strength are found in the subpolar oceans. Deep convection in the northern North Atlantic becomes significantly more vigorous, which in turn leads to an increase in the Atlantic Meridional Overturning Circulation (AMOC) by as much as 55%. As a result of the strengthened horizontal gyre circulations and the AMOC, the maximum global northward heat transport increases by almost 50%. Results from this study show that synoptic atmospheric phenomena such as weather systems play a vital role in driving the global ocean circulation and heat transport, and therefore should be properly accounted for in paleo and future climate studies.

1. Introduction

Air-sea momentum and energy fluxes play a fundamental role in driving the circulations in both the oceans and atmosphere (e.g., Gill 1982; Wunsch and Ferrari 2004). Because of this, large efforts have been spent on improving the quality of air-sea flux datasets and forcing formulations (e.g., Large and Yeager 2009; Griffies et al. 2009; Brodeau et al. 2010; Danabasoglu et al. 2014). Recent studies show that a significant fraction of air-sea turbulent fluxes are caused by transient atmospheric phenomena such as synoptic weather systems, owing to the nonlinear nature of air-sea bulk formulas (e.g., Ponte and Rosen 2004; Hughes et al. 2012; Zhai et al. 2012; Zhai 2013). For example, the bulk formula for computing surface wind stress states that the wind stress depends quadratically on the wind (e.g., Zhai et al., 2012):

$$\boldsymbol{\tau} = \rho_a c_d |\mathbf{U}_{10} - \mathbf{u}_o| (\mathbf{U}_{10} - \mathbf{u}_o), \tag{1}$$

where $\boldsymbol{\tau}$ is the surface wind stress, ρ_a is air density at the sea surface, c_d is the drag coefficient that depends on wind speed and stability of the atmospheric boundary layer, $\mathbf{u}_0$ is the ocean surface velocity, $\mathbf{U}_{10}$ is the 10-m wind velocity. As a consequence of this quadratic dependence, time-varying winds do not average out, but contribute towards the time-mean wind stress.

It has long been recognized that neglecting high-frequency winds can lead to large errors in the estimate of surface wind stress (e.g., Esbenson and Reynolds 1981; Thompson et al. 1983; Hanawa and Toba 1987; Ledvina et al. 1993; Gulev 1994). For example, Gulev (1994) found that the time-mean wind stress at Ocean Weather Stations in the mid-west North Atlantic could be underestimated by about 30% if the

the 10-day averaged winds, rather than 3-hourly winds, were used in (1). While most of the previous studies focused on the biases introduced in the estimate of surface fluxes when time-averaged meteorological observations were used in the bulk formulas, a few recent studies have made use of such biases to highlight the role of high-frequency synoptic winds in air-sea momentum and energy exchanges (e.g., Ponte and Rosen 2004; Zhai et al. 2012; Zhai 2013; Zhai and Wunsch 2013). For example, Zhai et al. (2012) computed power input to the ocean general circulation by the monthly and 6-hourly winds respectively, and found that the net wind power input increases by over 70% when the 6-hourly winds are used in the stress calculation. Zhai and Wunsch (2013) further showed that variability of wind power input to the subpolar North Atlantic is also mostly caused by variability of synoptic winds, with greater power input in years of enhanced storm activities.

Synoptic weather systems are also known to have a large influence on air-sea heat fluxes (e.g., Levina et al. 1993; Gulev 1994; Hughes et al. 2012). For example, Hughes et al. (2012) found that the monthly-mean latent heat fluxes can be underestimated by as large as 90 W m^{-2} in the western boundary current regions during winter and by more than 40 W m^{-2} in synoptically active portions of the tropics when the monthly-averaged winds, temperatures and humidities are used in the bulk formula for calculating latent heat fluxes. Using a simple one-dimensional mixed layer model, they went on to show that latent heat fluxes associated with synoptic weather systems are capable of reducing the sea surface temperature (SST) at a rate of over 1 ^{o}C $month^{-1}$ in the North Atlantic and Pacific mid-latitudes. Recent development of advanced probability distributions of observed sea surface wind speeds (Monahan 2006a,b) and turbulent heat fluxes (Gulev and Belyaev 2012) further highlighted the importance of intense synoptic cyclone activities in contributing to the averaged air-sea fluxes of momentum and heat as well as in causing extreme flux values at mid- and subpolar latitudes. For example, Gulev and Belyaev (2012) analyzed sensible and latent turbulent heat fluxes computed from the 6-hourly NCEP-NCAR reanalysis state variables and found that extreme turbulent heat fluxes associated with cold air outbreaks can be as large as 1500-2000 W m^{-2} (for the 99th percentile) in the subpolar latitudes and western boundary current regions, highlighting the importance of properly resolving the tail probability distribution of turbulent fluxes.

Despite the fact that synoptic atmospheric forcing plays an important role in determining air-sea momentum and energy fluxes, its impact on ocean circulation remains, however, rather poorly understood. So far, there have been only a limited number of studies investigating the impact of mesoscale and synoptic-scale atmospheric phenomena on the ocean (Condron and Renfrew 2013; Jung et al. 2014; Holdsworth and Myers 2015). Condron and Renfrew (2013) compared model simulations with and without a parameterization of mesoscale polar lows, and found that the parameterized polar lows can lead to enhanced heat loss and stronger deep convection in the Nordic Seas, which in turn leads to a spin-up of the North Atlantic subpolar gyre circulation and a larger northward transport of heat into the Nordic Seas. Jung et al. (2014) investigated the oceanic response to mesoscale atmospheric forcing using a coarse-resolution global sea ice-ocean model. They found that mesoscale features in atmospheric forcing fields such as fronts and mesoscale cyclones leads to a strengthening of the mean horizontal wind-driven gyre circulation of about 5-10% and a slight strengthening of the Atlantic meridional overturning circulation (AMOC). More recently, Holdsworth and Myers (2015) studied the influence of high-frequency atmospheric forcing on the circulation and deep convection of the Labrador Sea by comparing model simulations with and without high-frequency atmospheric phenomena. They found that, in the absence of high-frequency atmospheric phenomena, the strength of the AMOC decreased by about 25%, and the average maximum mixed layer depth (MLD) in the Labrador Sea decreased by between 20% and 100%.

Although progress has been made in recent years, there still lack systematic studies of the impact of synoptic-scale weather systems on the global ocean circulation. Here we investigate this problem using a start-of-the-art global ocean circulation model at eddy-permitting resolution for the first time. It is worth pointing out that our study is very different from previous studies on the influence of time-varying momentum and heat flux forcing on the ocean (e.g., Hakkinen 1999; Eden and Willebrand 2001; Gulev et al. 2003; Lozier et al. 2008; Zhai et al. 2014) where turbulent fluxes taken from reanalysis products are directly used to force ocean models. As discussed earlier, transient atmospheric phenomena such as synoptic weather systems not only cause air-sea momentum and heat fluxes to vary in time but also significantly contribute towards the time-mean fluxes owing to the strong nonlinear dependence of these turbulent fluxes on meteorological variables. Therefore, models forced directly by time-varying momentum and heat fluxes only capture part of the effect of transient atmospheric phenomena on the ocean.

The paper is organized as follows. We begin in Section 2 with a brief description of the model setup and experimental design. The impact of synoptic atmospheric phenomena on air-sea turbulent fluxes and the global ocean response to these fluxes are described and discussed in Section 3. We close with a summary and discussion of our results in Section 4.

2. Numerical model experiments

The model used in this study is the MIT general circulation model (MITgcm; Marshall et al. 1997a, b) in the ECCO2 state estimate configuration (the Estimating the Circulation and Climate of the Ocean, phase 2, high-resolution global-ocean and sea ice data synthesis). The model employs a cube-sphere grid projection, which permits relatively even grid spacing throughout the domain and avoids polar singularities (Adcroft et al. 2004). The mean horizontal grid spacing of the model is roughly 18 km (~1/6^{o} in latitude), i.e., eddy-permitting, and there are 50 unevenly spaced vertical levels whose thickness increases from 10 m near the surface to 450 m near the ocean bottom. The ocean model is coupled with the MITgcm sea ice model that simulates a viscous-plastic rheology (Losch et al. 2010). The model is run with optimized control parameters that are used to reduce the model-data misfit by the Green function approach (Menemenlis et al. 2005a, b, 2008). We refer readers to Menemenlis et al. (2008) and Chen (2013) for more details about the configuration of

ECCO2 state estimate.

Two model experiments are conducted. The control experiment (Exp-6HR) is forced by 6-hourly atmospheric data taken from the Japanese 55-year Reanalysis (JRA-55) dataset for the period of 1979-2012 (Kobayashi et al. 2015). JRA-55 is based on a new data assimilation and prediction system that improves many deficiencies found in the first Japanese reanalysis (JRA-25), and its forcing field is further optimized by the Green function approach (Menemenlis et al. 2005b). The input atmospheric data used in Exp-6HR include 6-hourly net long-wave radiation, net short-wave radiation, humidity, 2-m air temperature, precipitation, and 10-m wind velocity. Surface latent and sensible heat fluxes are calculated using the bulk aerodynamic formulas in the following form (Large and Pond, 1982):

$$Q_L = \rho_a L_e c_L V_{10}(q_s - q_a) \qquad (2)$$

$$Q_S = \rho_a c_p c_S V_{10}(T_0 - T_a) \qquad (3)$$

where c_L and c_S are stability-dependent bulk transfer coefficients for water vapor and heat respectively, L_e is the latent heat of evaporation, c_p is the specific heat of air, q_a is the specific humidity, q_s is the saturated specific humidity at SST, T_a and V_{10} are, respectively, the air temperature and wind speed at a height of 10 m and T_0 is the SST.

In order to isolate the influence of synoptic atmospheric forcing, we conduct another experiment (Exp-MON) where we exclude forcing associated with synoptic atmospheric phenomena such as weather systems by monthly averaging the atmospheric variables (e.g., air temperature and 10-m winds) prior to the calculation of surface fluxes[1]. As such, contributions of synoptic atmospheric systems to both the time-mean and time-varying surface fluxes are removed in this experiment. The difference between Exp-6HR and Exp-MON is then used to show the impact of synoptic atmospheric forcing on the ocean. Both experiments are initialized with the same climatology and integrated for 34 years from 1 January 1979 to 31 December 2012. Restoring boundary conditions are used in neither of the two experiments in order to allow the model to evolve freely under different atmospheric forcings. Unless otherwise stated, model output averaged from the last ten years at 18 km resolution is used for this study.

3. Results

a. Air-sea fluxes

1) Momentum flux

Surface wind stresses averaged over the last ten years from Exp-6HR and Exp-MON are shown in Figs. 1a and b, respectively. While the spatial distributions of the time-mean wind stresses are similar between these two experiments, the magnitude is much greater in Exp-6HR, particularly in the storm track regions at mid and high latitudes where the synoptic wind variability is strong (Fig. 1c). For example, the magnitude of the time-mean wind stress increases by almost 100% from 0.03 N m^{-2} to 0.06 N m^{-2} when averaged over the Gulf Stream region (70°W-0°, 35°N-65°N), by about 67% from 0.03 N m^{-2} to 0.05 N m^{-2} over the Kuroshio Extension region (165°E-120°W, 30°N-60°N), and by about 60% from 0.06 N m^{-2} to 0.1 N m^{-2} in the

[1] In doing this, any atmospheric phenomena that are resolved by the JRA-55 reanalysis data and have periods less than a month are filtered out, including tropical and extratropical cyclones, weather fronts as well as part of the intraseasonal variability associated with planetary wave activities.

Southern Ocean (40°S-70°S). At low latitudes where the monthly winds account for the majority of wind variability, the difference between wind stresses in the two experiments is generally small. Furthermore, co-variances of synoptic wind variability are found to explain most of the increase in the mean wind stress seen in Fig. 1c, while the variable drag coefficient makes a non-negligible contribution in the storm track regions, particularly in the Southern Ocean (see also Zhai 2013).

Figure 2a shows the probability density distribution of wind speeds at mid- and low-latitude North Atlantic in the two experiments. At mid latitudes, the wind speed calculated from 6-hourly winds exhibits a heavy tail distribution where the frequency of occurrence drops slowly towards higher wind speed, but such tail effect is significantly reduced for wind speed calculated from monthly winds (Monahan 2006a,b). In contrast, wind speeds calculated from 6-hourly and monthly winds at low latitudes are highly comparable to each other. Similar differences in wind speed distributions between mid and low latitudes are also found for different seasons. As a result, the wind stress distribution at mid latitudes in Exp-6HR is shifted strongly towards higher wind stress comparing to that in Exp-MON, but there are little differences between wind stress distributions at low latitudes between the two experiments (Fig. 2b). This further confirms the important role of synoptic wind variability in modulating the magnitude of surface wind stress at mid and high latitudes, but not at low latitudes. The level of increase in the time-mean wind stress shown in Fig. 1c when the synoptic winds are included in the stress calculation is similar to that found by Zhai et al. (2012), but much greater than that found by Jung et al. (2014). The difference between the present study and Jung et al. (2014) can be largely explained by the different focuses of the two studies: Jung et al. (2014) focused on the influence of *mesoscale* atmospheric phenomena, while the present study focuses on that of *synoptic* atmospheric phenomena. Atmospheric motions at synoptic scales are known to be much more energetic than those at mesoscales (e.g., Naström et al. 1984).

Changes of the time-mean wind stress owing to the presence of synoptic atmospheric phenomena have ramifications for wind vorticity forcing of the ocean general circulation. Figure 3 shows that, when the synoptic winds are included in the stress calculation, the magnitude of the time-mean wind stress curl increases almost everywhere regardless of its polarity. Not surprisingly, this increase is most pronounced at mid and high latitudes, particularly near Greenland and Antarctica, where the synoptic wind variability is particularly strong, which, through nonlinearity of the bulk formula, contributes significantly to the time-mean wind stress (Fig. 3c). It will be shown later that changes in the wind stress curl result in changes in the strength of horizontal wind-driven gyre circulations.

2) Heat and freshwater fluxes

The time-mean net surface heat fluxes in Exp-6HR and Exp-MON are shown in Figs. 4a and b and their difference (Exp-6HR minus Exp-MON) in Fig. 4c. Heat fluxes in both experiments are characterized by heat gain at low latitudes and significant heat loss in the western boundary current regions, the subpolar North Atlantic and the Nordic Seas. When synoptic atmospheric forcing is included, heat loss becomes much more pronounced in Exp-6HR, particularly in the North Atlantic (Fig. 4c). For example, heat loss averaged over the North Atlantic increases from ~19 W m^{-2} in Exp-MON to ~39 W m^{-2} in Exp-6HR, and that over the North Pacific from ~24 W m^{-2} to ~36 W m^{-2}. There is also a moderate increase in heat loss in the Agulhas Current retroflection region and a slight increase in heat gain in the tropics in Exp-6HR comparing to Exp-MON. Similar to the wind stress, Figure 2c shows that synoptic phenomena generally shift the distribution of surface heat flux towards more extreme values at mid latitudes, but have little effects on the distribution of surface heat flux at low latitudes (Gulev and Belyaev 2012). Differences in heat loss between the two experiments in the western boundary current regions and higher latitudes mainly result from synoptic atmospheric phenomena such as cold winter air outbreaks that are present in Exp-6HR but absent in Exp-MON (e.g., Hughes et al. 2012; Condron and Renfrew 2013; Jung et al. 2014). Further calculations show that differences in latent heat flux explain most of the differences in net heat flux seen in Fig. 4c and variable transfer coefficients make an important contribution towards these differences (not shown). It is worth pointing out that changes in ocean circulation can also play a role in modulating these differences, since surface heat fluxes in these model experiments are not prescribed but depend on the modeled SST.

Figure 5 shows the distributions of time-mean net surface freshwater fluxes in Exp-6HR and Exp-MON as well as the difference between them. The overall pattern and magnitude of freshwater fluxes are similar between these two experiments as well as similar to those in other studies (e.g., Stammer et al. 2004). Large freshwater input to the ocean is found in the Inter-tropical Convergence Zone (ITCZ) and also in high latitudes, while evaporation exceeds precipitation in the subtropics (Figs. 5a and b). Sea ice melting/freezing makes a significant additional contribution to the net freshwater flux in high latitudes. For example, there is a narrow stripe of intense freshwater input along the eastern Greenland associated with sea ice melting, similar to that found in Stammer et al. (2004). Figure 5c shows that including synoptic atmospheric forcing results in enhanced evaporation over the majority of the global ocean due to the increase in wind speed.

b. Wind power input and eddy kinetic energy

Mechanical energy input to the ocean by atmospheric winds is a major energy source for driving the ocean circulation and maintaining ocean stratification (Wunsch and Ferrari 2004). Figure 6 shows the distributions of global wind power input to the ocean in the two experiments and the difference between them. Wind power input, P, is calculated here using $P=\overline{\tau\cdot u}$, where τ is the surface wind stress, u is the ocean surface velocity that includes both geostrophic and ageostrophic components, and the overbar denotes a 10-year time average. Large positive values of P are found in the Southern Ocean, Gulf Stream, Kuroshio Extension, and also the tropics in both experiments, consistent with previous studies (e.g., Huang et al. 2006; von Storch et al. 2007). When the synoptic winds are included in the stress calculation, P is strongly enhanced, particularly in the storm track regions where the synoptic winds make large contributions to the time-mean wind stress. Over 80% of P at high northern latitudes, for example, can be explained by winds associated with synoptic atmospheric phenomena. In the tropics, there are alternating bands of positive and negative wind power changes due to changes in wind forcing as well as meridional shift of the zonal currents under different forcings. Integrated globally, P increases by almost 50% from 0.89 TW (1 TW=10^{12} W) in Exp-MON to 1.32 TW in Exp-6HR. In comparison, Huang et al. (2006) estimated P to be about 1.16 TW for the period of 1993-2003 using a coarse-resolution ocean circulation model driven by NCEP-NCAR reanalysis wind stresses.

Wind power input that goes into the geostrophic motions in the ocean is often of greater interest and is therefore more frequently diagnosed (Wunsch 1998; Hughes and Wilson 2008; Scott and Xu 2009; Zhai et al. 2012; Zhai 2013). This is because the majority of wind power input to surface waves and other ageostrophic motions is dissipated within the surface layer and as such is not available for deep ocean mixing (e.g., von Storch et al. 2007; Zhai et al. 2009). Following Wunsch (1998), wind power input to the geostrophic ocean circulation, P_g, is diagnosed using $P_g = \overline{\tau \cdot u_g}$, where u_g is the surface geostrophic velocity calculated from the sea surface height field. The spatial distributions of P_g in both experiments are similar to that found in previous studies (e.g., Wunsch 1998; Hughes and Wilson 2008; Zhai et al. 2012), with the majority of P_g entering the Southern Ocean (Figs. 7a and b). However, regions of both positive and negative P_g become more pronounced when the synoptic winds are included. Integrated globally, P_g increases by about 47% from 0.47 TW in Exp-MON to 0.69 TW in Exp-6HR. The net P_g in Exp-6HR is comparable to, although slightly smaller than, the 0.76 TW estimated by Hughes and Wilson (2008), but is significantly smaller than the 0.88 TW estimated by Wunsch (1998). This difference in the estimates of P_g is expected since including ocean surface velocity in the wind stress calculation can lead to a noticeable reduction in wind power input[2] (e.g., Duhaut and Straub 2006; Hughes and Wilson 2008; Zhai et al. 2012) and this effect is accounted for in the present study and Hughes and Wilson (2008), but not in Wunsch (1998).

When assessing the role of synoptic wind variability in power input from observations, changes in ocean circulation are often neglected in the power calculation when different types of winds (e.g. 6-hourly or monthly) are used (Zhai et al. 2012; Zhai and Wunsch 2013). The error associated with this steady ocean circulation assumption is unknown. Here we test this assumption by calculating an additional P_g using the inner product of τ from Exp-MON and u_g from Exp-6HR. The resulting P_g (Fig. 7c) has a net value of 0.48 TW and a pattern that is almost indistinguishable from that in Exp-MON (Fig. 7b), which confirms that the steady ocean circulation assumption used in previous studies is adequate at present levels of accuracy. In other words, when the synoptic winds are included in the stress calculation, it is the changes of wind stress, not changes of ocean circulation, that dominate the changes of wind power input to the ocean seen in Figs. 6 and 7.

There is increasing evidence in support of the notion that the majority of wind power input to the large-scale geostrophic circulation is balanced by eddy generation

[2] This is because the wind stress depends on the relative motion between the atmosphere and the surface ocean. When the wind is aligned with the ocean surface current, the wind stress is smaller than in the motionless ocean case due to smaller relative motion and hence the wind does less positive work. When the wind opposes the current, the stress is larger and hence the wind does more negative work. Therefore, including ocean surface velocity in the stress calculation leads to a systematic reduction in the wind power input to the ocean.

through instabilities of the mean flow (e.g., Gill et al. 1974; Wunsch 1998; Zhai and Marshall 2013). We therefore expect the large difference in P_g between Exp-6HR and Exp-MON to lead to considerable differences in the strength of eddy activities. Figure 8 shows the spatial distribution of surface eddy kinetic energy (EKE) in the two experiments. EKE here is defined as $\overline{(u'^2 + v'^2)}/2$, where primes denote deviations from the monthly mean and the overbar again denotes a 10-year time average. In both experiments, large values of EKE are found to concentrate in the western boundary current regions, the Southern Ocean, and also in the tropics, i.e., regions where the ocean is known to be subject to strong baroclinic/barotropic instabilities (e.g., Stammer 1998; Smith 2007). As expected, when the synoptic wind forcing is included in the model, the simulated EKE increases almost everywhere. For example, surface EKE averaged over the North Atlantic and the Southern Ocean in Exp-6HR almost doubles that in Exp-MON. Integrated over the global ocean, EKE increases by almost 50% from 0.63 EJ (1 EJ=10^{18} J) in Exp-MON to 0.94 EJ in Exp-6HR. The similar percentage increase in wind power input and EKE found here adds further support to the ocean energy pathway hypothesized originally by Gill et al. (1974), that is, wind power input to the large-scale ocean circulation is balanced by production of ocean eddies through instability of the mean flow.

c. Gyre circulation and ACC transport

The overall patterns of the time-mean barotropic streamfunctions in Exp-6HR (Ψ_{6hr}) and Exp-MON (Ψ_{mon}) are very similar (Figs. 9a and b), with both characterized by anticyclonic subtropical gyre circulations, cyclonic subpolar gyre circulations as well as the eastward-flowing Antarctic Circumpolar Current (ACC). When synoptic atmospheric forcing is included in the model, the simulated horizontal gyre circulations generally increase in their strength (Fig. 9c; see Table 1 for a list of the strength of the main ocean gyres). For example, the mean strength of the subtropical gyre circulation in the North Atlantic increases by about 9% from 80.2 Sv (1 Sv = 10^6 $m^3 s^{-1}$) in Exp-MON to 87.3 Sv in Exp-6HR and that in the South Atlantic by about 15% from 70.1 Sv in Exp-MON to 80.4 Sv in Exp-6HR. The subtropical gyre circulations in the North and South Pacific are also found to strengthen by a similar amount. The subpolar gyres, on the other hand, increase in strength much more than the subtropical gyres. For example, the mean strength of the North Atlantic subpolar gyre circulation increases by about 46% from 36.3 Sv in Exp-MON to 52.9 Sv in Exp-6HR, closer to the observed value of 48.8 Sv (Reynaud et al. 1995). Similar changes in the strength of the North Atlantic subpolar gyre were reported by Holdsworth and Myers (2015) where they found the mean value of the gyre strength increases from 39 Sv to 52 Sv when the high-frequency atmospheric forcing was taken into account. In the North Pacific, the strength of the simulated subpolar gyre circulation is almost doubled from 15.5 Sv in Exp-MON to 30.3 Sv in Exp-6HR.

A few recent studies (e.g., Wunsch 2011; Thomas et al. 2014) show that Sverdrup balance provides a quantitatively useful measure of the meridional transport in the interior of the subtropical oceans. The increase in the strength of the simulated subtropical gyre circulations in Exp-6HR is consistent with the Sverdrup theory, where the strengthened wind stress curl owing to contributions from the synoptic winds leads to greater depth-integrated meridional transport. The greater difference in gyre strength at high latitudes between the two experiments can be explained by the greater contribution of synoptic winds to the time-mean wind stress at these latitudes (Fig. 3), although enhanced heat loss in Exp-6HR may also play a role (Fig. 4; Wang and Meredith 2008; Wang 2013). Again, changes of the horizontal wind-driven gyre circulations found in our study are greater than those in previous studies focusing on the role of mesoscale atmospheric forcing (e.g., Condron and Renfrew 2013; Jung et al. 2014), since atmospheric motions at synoptic scales tend to be much more energetic than those at mesoscales.

Figure 10a shows the time series of ACC transport at Drake Passage in Exp-6HR and Exp-MON. The negative trends in ACC transports in both experiments are likely to be caused by model drift associated with declining Antarctic Bottom Water formation. Focusing therefore on the differences between the two experiments, we find that the mean ACC transport in Exp-6HR (115.8 Sv) is not very different to that in Exp-MON (111.5 Sv), despite that the Southern Ocean wind stress in Exp-6HR is much stronger than that in Exp-MON (Fig. 1). This insensitivity of ACC transport to wind stress changes found in our eddy-permitting model appears to be consistent with the eddy saturation phenomenon discussed in a number of studies (e.g., Straub 1993; Meredith and Hogg 2006; Wang et al. 2011; Munday et al. 2013; Munday and Zhai 2015). It has been shown that, under an eddy-saturated state, increases in the northward Ekman transport caused by stronger westerly winds are compensated by enhanced southward eddy fluxes, resulting in little changes in isopycnal slopes and

ACC transport. Consistent with this eddy saturation argument, Figure 10b shows that although the zonal mean isopycnal surfaces across the ACC tilt slightly more in the upper 300 m in Exp-6HR than Exp-MON, there is virtually no difference between the two experiments below 300 m. Eddy saturation may also help to explain why Jung et al. (2014) found a greater increase in ACC transport in their coarse-resolution ocean model that does not resolve eddies, despite the smaller increase in the Southern Ocean wind stress associated with mesoscale atmospheric phenomena. There are some differences between interannual variability of ACC transports in the two experiments, which are most likely due to intrinsic variability of the ACC (e.g., Wilson et al. 2015), rather than differences in external forcing, since the standard deviations of the time series of ACC transports in the two experiments are almost identical (10.45 Sv for Exp-6HR and 10.44 Sv for Exp-MON respectively).

d. Deep convection and AMOC

Following Holdsworth and Myers (2015), we now investigate the impact of synoptic atmospheric forcing on the MLD and the intensity of deep convection at high latitudes. The MLD in the ECCO2 state estimate is defined, following the algorithm of Kara et al. (2000, 2003), as the depth at which the density differs from that at the surface by an amount of $\Delta\sigma_t = \sigma_t(T+\Delta T, S, P_A) - \sigma_t(T, S, P_A)$, where T is temperature, S is salinity, and P_A is the atmospheric pressure. The density criterion, $\Delta\sigma_t$, is determined by the optimal value of ΔT = 0.8°C estimated by Kara et al. (2000) to best fit two observational datasets.

Figure 11 shows the distribution of winter MLDs in Exp-6HR and Exp-MON

(March-mean for the Northern Hemisphere and September-mean for the Southern Hemisphere) and the difference between them. The MLDs in both experiments are characterized by relatively shallow surface mixed layers at low latitudes and deep mixed layers at mid and high latitudes. When synoptic atmospheric forcing is included, the MLD increases significantly at high latitudes, particularly in the northern North Atlantic, the Nordic Sea, and the Southern Ocean (Fig. 11c). Figure 12a shows the time series of March-mean MLD within the 3000 m isobath in the Labrador Sea (bounded to the east and south by 40^{o}W and 49^{o}N respectively) simulated in the two experiments. The average March-mean MLDs in the Labrador Sea are 934 m in Exp-MON and 2750 m in Exp-6HR respectively. The greater winter MLD in Exp-6HR is associated with the much stronger deep convection triggered by synoptic atmospheric forcing in this experiment. As shown in Figs. 12b and c, the magnitudes of the March-mean surface heat loss and cyclonic wind stress curl are much greater in Exp-6HR than in Exp-MON. Averaged over the Labrador Sea, including synoptic atmospheric forcing enhances the surface heat loss from 95 W m^{-2} in Exp-MON to 348 W m^{-2} in Exp-6HR, and strengthens the cyclonic wind stress curl from 4.1×10^{-7} N m^{-3} in Exp-MON to 9.0×10^{-7} N m^{-3} in Exp-6HR. The strengthened cyclonic wind stress curl in Exp-6HR brings the density surfaces in the Labrador Sea further up towards the surface through the action of Ekman suction, which results in a stronger cyclonic circulation and a weaker vertical stratification than in Exp-MON (Marshall and Schott 1999). This further preconditioning then makes it easier for the enhanced surface heat loss in Exp-6HR to punch through the weak stratification and trigger deep-reaching convection seen in Fig. 12a. Changes of the MLD in the Labrador Sea found in this study when synoptic atmospheric forcing is included are much greater than those reported by Holdsworth and Myers (2015), which may be related to different strengths and patterns of deep convection modeled in these two studies. We note there are two issues that may lead to biases in our modeled MLD in the Labrador Sea: 1) the model is only eddy-permitting, particularly at subpolar latitudes, so the role the eddies play in the restratification process after deep convection events is very likely to be underestimated; 2) In the absence of surface salinity restoring, the modeled surface salinity in the Labrador Sea tends to be higher than that from the World Ocean Atlas (not shown), which can again affect the strength of modeled convective activities.

Changes in the intensity of deep convection in the North Atlantic are likely to lead to changes in the strength of the AMOC, as shown by a number of previous studies (e.g., Eden and Willebrand 2001; Lozier et al. 2008; Zhai et al. 2014). The AMOC is calculated here by zonally integrating the meridional velocity across the Atlantic basin from its western boundary (x_W) to eastern boundary (x_E) and from the ocean bottom at *z*=-*h* upward: $\psi(y,z,t) = \int_{-h}^{z}\int_{x_W(y,z)}^{x_E(y,z)} v(x,y,z,t)dxdz$. The strength of the AMOC is then defined as the maximum value of ψ with depth. The AMOCs in both Exp-6HR and Exp-MON exhibit the familiar structure in the meridional/depth plane (e.g., Wunsch and Heimbach 2013): northward transport of light water replaced by a southward transport of dense water that is recently ventilated at high latitudes in the North Atlantic (Figs. 13a and b). There is also a second, much weaker, cell in the deep ocean associated with the northward export of the Antarctic Bottom Water. As shown in Fig. 13c, when synoptic atmospheric forcing is included, the strength of the simulated AMOC increases coherently across all latitudes by as much as 5 Sv, and meanwhile the AMOC also expands downwards. There appear to be little changes associated with the second cell in the deep ocean.

Since April 2004, the strength and vertical structure of the AMOC have been continuously monitored at 26.5^{o}N by the transatlantic RAPID array (Rayner et al. 2011). Figure 14 shows the time series of the AMOCs at 26.5^{o}N simulated by the two experiments as well as the AMOC measured by the RAPID array. After the initial adjustment of a few years, the two simulated AMOCs diverge, with the AMOC in Exp-6HR consistently stronger than that in Exp-MON. For example, the AMOCs at 26.5^{o}N in Exp-MON and Exp-6HR over the period of 2004-2012 are 9.57±2.63 Sv and 14.79±3.02 Sv, respectively, whereas the AMOC measured by the RAPID array over the same period is 17.09±3.56 Sv. In addition, the modeled AMOC in Exp-6HR is found to be significantly correlated with the RAPID observation, while the modeled AMOC in Exp-MON is not. Therefore, including synoptic atmospheric forcing in the model brings both the mean and variability of the simulated AMOC closer to the observed values. Interestingly, Exp-6HR reproduces the observed rapid drop of the AMOC transport in 2010 and its recovery afterwards, while this feature is completely missed by Exp-MON. The magnitude of the increase of the AMOC at 26.5^{o}N in our model when synoptic atmospheric forcing is included is comparable to that found by Holdsworth and Myers (2015), although the strength of the time-mean AMOCs in the two studies are very different.

e. Meridional heat transport

One of the key roles that the oceans play in the climate system is to transport heat to high latitudes. As shown in previous sections, including synoptic atmospheric forcing leads to large changes in the strength of both the horizontal wind-driven gyre circulation and the AMOC. Now we investigate the effect of these circulation changes on the meridional heat transport in the ocean.

The overall structures of the meridional ocean heat transport in both Exp-6HR and Exp-MON are similar to those inferred from the observations (e.g., Trenberth and Caron 2001; Ganachaud and Wunsch 2003): poleward in the Pacific and Indian Oceans where heat transport by the wind-driven circulation dominates and northward everywhere in the Atlantic Ocean where heat transport by the AMOC dominates (Fig. 15). However, in the absence of synoptic atmospheric forcing, the magnitude of meridional heat transport in each ocean basin decreases considerably. In the Atlantic Ocean, the maximum northward heat transport in Exp-6HR is 0.92 PW (1 PW= 10^{15}W) at 25°N, which is comparable to the 1.07±0.26 PW estimated by Macdonald (1998) but lower than the 1.27±0.15 PW estimated by Ganachaud and Wunsch (2003). In comparison, the maximum northward heat transport in Exp-MON is only 0.66 PW, representing a 28% decrease in magnitude. Consistent with the dominant role played by the AMOC in meridional heat transport in the Atlantic basin, the percentage decrease in the maximum northward heat transport when synoptic atmospheric forcing is excluded is roughly mirrored by the percentage decrease in the AMOC at similar latitudes. In equilibrium, horizontal convergence/divergence of the meridional ocean heat transport is balanced by the net surface heat loss/gain. The sharper drops in meridional heat transport at around 40^{o}N and 60^{o}N in Exp-6HR are associated with the much greater heat loss over the Gulf Stream region and at higher latitudes owing to the presence of synoptic atmospheric forcing (Fig. 4).

Poleward heat transports in both the Pacific and Indian Oceans are also reduced when synoptic atmospheric forcing is excluded. For example, the maximum northward heat transport in the North Pacific is 0.5 PW in Exp-6HR but only about 0.33 PW in Exp-MON, that is, a 34% decrease. The total heat transports in the combined Indo-Pacific Oceans at 24^{o}N, 18^{o}S and 30^{o}S in Exp-6HR are 0.39 PW, -1.71 PW and -1.4 PW, respectively, which compare reasonably well with the 0.52±0.2 PW, -1.6±0.6 PW and -0.9±0.3 PW estimated by Ganachaud and Wunsch (2003) and those estimated by the atmospheric residual method (e.g., Trenberth and Caron 2001). When synoptic atmospheric forcing is excluded, meridional heat transports at 24^{o}N, 18^{o}S and 30^{o}S reduce to 0.27 PW, -1.58 PW and -1.26 PW in Exp-MON respectively.

Globally, both experiments show an asymmetry across the equator: poleward heat transport is much greater in the Northern Hemisphere than in the Southern Hemisphere, as is also found in observations (e.g., Trenberth and Caron 2001; Ganachaud and Wunsch 2003). The smaller heat transport in the Southern Hemisphere results from cancellations between the northward heat transport in the South Atlantic and southward heat transport in the South Pacific and Indian Oceans, whereas heat transports in both the North Atlantic and North Pacific are northward. In Exp-6HR, the maximum poleward heat transport in the Northern Hemisphere reaches 1.5 PW at about 20^{o}N, over three times of that in the Southern Hemisphere (at 15^{o}S). These peaks values compare reasonably well with the 1.5±0.3 PW estimated by Macdonald and Wunsch (1996) and 1.8±0.3 PW by Ganachaud and Wunsch (2003) at 24^{o}N and with the -0.8±0.6 PW by Ganachaud and Wunsch (2003) at 19^{o}S. When synoptic atmospheric forcing is excluded in the model, the maximum northward heat transport in the Northern Hemisphere reduces to about 1 PW in Exp-MON, i.e., only two-thirds of that in Exp-6HR. In contrast, meridional heat transport in the Southern Hemisphere remains largely unchanged. This is again due to near-cancellation between reductions in both the northward heat transport in the South Atlantic and southward heat transport in the Indo-South Pacific Oceans in Exp-MON.

4. Summary and discussion

Owing to the nonlinear nature of air-sea turbulent fluxes, transient atmospheric phenomena such as synoptic weather systems not only cause air-sea fluxes to vary in time but also contribute significantly towards the time-mean fluxes. Here the role of synoptic atmospheric systems in air-sea fluxes and the impact of these fluxes on the mean ocean circulation are investigated using a global eddy-permitting ocean-sea ice model. By comparing model simulations with and without synoptic atmospheric forcing, we find that

- Synoptic winds contribute significantly to the time-mean wind stress and its curl, particularly in the storm track regions at mid and high latitudes. Including synoptic atmospheric forcing strengthens the subtropical gyre circulations by about 10-15%, whereas even greater increases in gyre strength are found in the subpolar oceans. The ACC transport, on the other hand, remains relatively insensitive to changes in wind stress due to eddy saturation effect.

- When the synoptic winds are included in the stress calculation, wind power input to the ocean circulation increases by almost 50% from 0.89 TW to 1.32 TW and power input to the geostrophic motions increases by about 47% from 0.47 TW to 0.69 TW. We find that it is the changes of wind stress, not changes of ocean circulation, that dominate the increase in wind power input. The increase in power input subsequently leads to an increase in the global EKE by about 50% from 0.63 EJ to 0.94 EJ.
- Synoptic atmospheric forcing enhances surface heat loss and deepens the surface mixed layer at mid and high latitudes, particularly in the North Atlantic. It leads to more vigorous deep convection in the northern North Atlantic, which, in turn, strengthens the AMOC by as much as 55%.
- Strengthened AMOC and gyre circulations increase the magnitude of the meridional heat transport in each ocean basin. The maximum global northward heat transport increases by almost 50% from 1 PW to 1.5 PW when synoptic atmospheric forcing is included.

Results from our study show that synoptic atmospheric systems play a vital role in driving the global ocean circulation and heat transport. This implies that past and future climate studies need to properly account for changes in weather systems, not just the large-scale variations. Recent climate model studies project a significant increase in the amplitude and frequency of cyclones in the Southern Hemisphere, but a general decrease in the Northern Hemisphere (e.g., Chang et al. 2012). These projected changes in storm activities are likely to lead to considerable changes in air-sea momentum and heat fluxes, which can, in turn, influence global ocean circulation and heat transport. Synoptic weather systems are also found to affect the surface ocean properties such as the mixed layer depth and modulate the rate of Ekman pumping and the strength of the eddy field. As such, these weather systems may play an important role in the surface water mass transformation process and in determining the subsequent subduction rate (e.g. Marshall 1997; Gulev 2003).

It is worth emphasizing that our study is different from previous studies focusing on the influence of time-varying surface momentum and heat flux forcing caused by transient atmospheric phenomena (e.g., Hakkinen 1999; Eden and Willebrand 2001; Lozier et al. 2008; Zhai et al. 2014). As shown earlier, these transient atmospheric phenomena not only cause air-sea momentum and heat fluxes to vary in time but also contribute significantly towards the time-mean fluxes. Therefore, studies on the impact of weather systems on the ocean need to work with meteorological variables such as air temperature and 10-m winds, rather than directly with air-sea momentum and heat fluxes. In this paper we focus on the impact of synoptic weather systems on the ocean, which differs but complements recent studies on the impact of mesoscale atmospheric phenomena (Condron and Renfrew 2013; Jung et al. 2014; Holdsworth and Myers 2015). Finally, the atmospheric data used here is still of coarse resolution---it certainly misses many mesoscale atmospheric phenomena and may underestimate some of the synoptic features as well. As such, the present study is likely to underestimate the impact of synoptic atmospheric systems on air-sea exchanges.

Acknowledgement. This work is funded by a Royal Society International Exchanges Award (IE131025). XZ acknowledge additional support from the School of Environmental Sciences, University of East Anglia. ZW was supported by the China National Natural Science Foundation (NSFC) Project (41276200), by the Global Change Research Program of China (2015CB953904), by the Special Program for China Meteorology Trade (Grant No. GYHY201306020), by Program for Innovation Research and Entrepreneurship team in Jiangsu Province, and by a project funded by the Priority Academic Program Development of Jiangsu Higher Education Institutions (PAPD).

REFERENCES

Adcroft, A., J.-M. Campin, C. Hill, and J. Marshall, 2004: Implementation of an atmosphere- ocean general circulation model on the expanded spherical cube. *Mon. Wea. Rev.*, **132**, 2845- 2863, doi: http://dx.doi.org/10.1175/MWR2823.1.

Brodeau, L., B. Barnier, A.-M. Treguier, T. Penduff, and S. Gulev, 2010: An ERA 40-based atmospheric forcing for global ocean circulation models. *Ocean Modell.*, **31**, 88-104.

Chang, E. K. M., Y. Guo, and X. Xia, 2012: CMIP5 multimodel ensemble projection of storm track change under global warming, *J. Geophys. Res.*, **117**, D23118, doi:10.1029/2012JD01 8578.

Chen, R., 2013: Energy pathways and structures of oceanic eddies from the ECCO2 state estimate and simplified models. *Ph.D. thesis, Massachusetts Institute of Technology and Woods Hole Oceanographic Institution*, 206 pp.

Danabasoglu, G., and Co-authors, 2014: North Atlantic simulations in Coordinated Ocean-ice Reference Experiments phase II (CORE-II). Part I: Mean states. *Ocean Modell.,* **73**, 76-107.

Condron, A., and I. A. Renfrew, 2013: The impact of polar mesoscale storms on northeast Atlantic Ocean circulation, *Nat. Geosci*., **6**, 34-37, doi:10.1038/ngeo1661.

Duhaut T. H. A., and D. N. Straub, 2006: Wind stress dependence on ocean surface velocity: Implications for mechanical energy input to ocean circulation. *J. Phys. Oceanogr.*, **36**(2): 202-211.

Esbenson, S. K., and R. W. Reynolds, 1981: Estimating monthly averaged air-sea transfers of heat and momentum using the bulk aerodynamic method, *J. Phys. Oceanogr.*, **11**, 457-465.

Eden, C., and J. Willebrand, 2001: Mechanism of interannual to decadal variability of the North Atlantic circulation, *J. Climate*, **14**(10), 2266-2280.

Ganachaud, A. and C. Wunsch, 2003: Large-Scale Ocean Heat and Freshwater Transports during the World Ocean Circulation Experiment. *J. Climate*, **16**, 696-705.

Gill, A.E., J. S. A. Green, and A.J. Simmons, 1974: Energy partition in the large-scale ocean circulation and the production of mid-ocean eddies. *Deep-Sea Res*., **21**, 499-528.

Gill, A. E., 1982: Atmosphere-Ocean Dynamics, 662 pp., *Academic*, London.

Griffies, S. M., and Co-authors, 2009: Coordinated Ocean-ice Reference Experiments (COREs). *Ocean Modell*., **26**, 1-46.

Gulev, S. K., 1994: Influence of space-time averaging on the ocean atmosphere exchange estimates in the North Atlantic mid latitudes, *J. Phys. Oceanogr*., **24**, 1236-1255.

Gulev, S. K., 2003: Water mass transformation in the North Atlantic and its impact on the meridional circulation: Insights from an ocean model forced by NCEP-NCAR reanalysis surface fluxes. *J. Climate*, **16**, 3085-3110.

Gulev, S. K., and K. P. Belyaev, 2012: Probability distribution characteristics for surface air-sea turbulent heat fluxes over the global ocean. *J. Climate*, **25**, 184-206.

Hakkinen, S., 1999: Variability in the simulated meridional heat transport in the North Atlantic for the period 1951-1993. *J. Geophys. Res*., **104**, 10991-11007.

Hanawa, K., and Y. Toba, 1987: Critical examination of estimation methods of long-term mean air-sea heat and momentum transfers, *Ocean Air Interact.*, **1**, 79-93.

Holdsworth, A.M., and P. G. Myers, 2015: The Influence of High-Frequency Atmospheric Forcing on the Circulation and Deep Convection of the Labrador Sea. *J. Climate*, **28**, 4980–4996.

Huang, R. X., W. Wang, and L. L. Liu, 2006: Decadal variability of wind-energy input to the world ocean. *Deep-Sea Res*., **53**(1), 31-41.

Hughes, C. W., and C. Wilson, 2008: Wind work on the geostrophic ocean circulation: An observational study on the effect of small scales in the wind stress. *J. Geophys. Res*., **113**, doi: 10.1029/2007JC004371.

Hughes, P. J., M. A. Bourassa, J. J. Rolph, and S. R. Smith, 2012: Averaging related biases in monthly latent heat fluxes, *J. Atmos. Oceanic Technol.*, **29**, 974-986.

Jung, T., S. Serrar, and Q. Wang, 2014: The oceanic response to mesoscale atmospheric forcing, *Geophys. Res. Lett.*, **41**, 1255-1260, doi: 10.1002/2013GL059040.

Kara, A.B., P.A. Rochford, and H.E. Hurlburt, 2000: An optimal definition for ocean mixed layer depth. *J. Geophys. Res*., **105**, (C7), 803-16,821, doi: 10.1029/2000JC900072.

Kara, A.B., P.A. Rochford , and H.E. Hurlburt, 2003: Mixed layer depth variability over the global ocean. *J. Geophys. Res*., **108**, doi:10.1029/2000C000736.

Kobayashi, S., Y. Ota, Y. Harada, et al., 2015: The JRA-55 reanalysis: General specifications and basic characteristics. *J. Meteor. Soc. Japan*, **93**(1), 5-48.

Large, W. G., and S. Pond, 1981: Open ocean momentum flux measurements in moderate to strong winds. *J. Phys. Oceanogr*., **11**, 324-336.

Large, W. G., and S. Pond, 1982: Sensible and latent heat flux measurements over the ocean. *J. Phys. Oceanogr*., **12**, 464-482.

Large, W. G., and S. G. Yeager, 2009: The global climatology of an interannually varying air-sea flux data set. *Clim. Dyn*., **33**, 341-364.

Ledvina, D. V., G. S. Young, R. A. Miller, and C. W. Fairall , 1993: The effect of averaging on bulk estimates of heat and momentum fluxes for the tropical western Pacific Ocean, *J. Geophys. Res*., **98**, (C11), 211-20,217, doi: 10.1029/93JC01856.

Losch, M., D. Menemenlis, P. Heimbach, J. Campin, and C. Hill, 2010: On the formulation of sea-ice models. Part 1: Effects of different solver implementations and parameterizations. *Ocean Model.*, **33**, 129-144.

Lozier, M. S., S. Leadbetter , R. G. Williams, V. Roussenov, M. S. Reed, and N. J. Moore, 2008: The spatial pattern and mechanisms of heat-content change in the North Atlantic. *Science*, **319**(5864), 800-803, doi:10.1126/science.1146436.

Macdonald, A .M., and C. Wunsch, 1996: An estimate of global ocean circulation and heat fluxes. *Nature*, **382**(6590), 436-439, doi:10.1038/382436a0.

Macdonald, A. M., 1998: The global ocean circulation: A hydrographic estimate and regional analysis. *Progress in Oceanography*, **41**(3), 281-382.

Marshall, J., A. Adcroft, C. Hill, L. Perelman, and C. Heisey, 1997a: A finite-volume, incompres- sible Navier Stokes model for studies of the ocean on parallel computers. *J. Geophys. Res.*, **102**, 5753-5766, doi:10.1029/96JC02775.

Marshall, J., C. Hill, L. Perelman, and A. Adcroft, 1997b: Hydrostatic, quasi-hydrostatic, and nonhydrostatic ocean modeling. *J. Geophys. Res.*, **102**, 5733-5752, doi:10.1029/96JC02776.

Marshall J., and F. Schott, 1999: Open-ocean convection: Observations, theory, and models. *Rev. Geophys*, **37**(1), 1-64, doi:10.1029/98RG02739.

Menemenlis, D. et al., 2005a: NASA supercomputer improves prospects for ocean climate research. *Eos,Trans. Amer. Geophys. Union*, **86**, 89-96, doi: 10.1029/2005EO090002.

Menemenlis, D., I. Fukumori, and T. Lee, 2005b: Using Green's functions to calibrate an ocean general circulation model. *Mon. Wea. Rev.*, **133**, 1224-1240.

Menemenlis, D., J. Campin, P. Heimbach, C. Hill, T. Lee, A. Nguyen,M. Schodlock, and H. Zhang, 2008: ECCO2: High resolution global ocean and sea ice data synthesis. *Mercator Ocean Quarterly News letter*, **31**, 13–21.

Meredith, M. P., and A. M. Hogg, 2006: Circumpolar response of SouthernOcean eddy activity to a change in the southern annular mode. *Geophys. Res. Lett.*, **33**, L16608, doi:10.1029/2006G L 026499.

Monahan, A. H., 2006a: The probability distribution of sea surface wind speeds. Part I: Theory and sea winds observations. *J. Climate*, **19**, 497-450.

Monahan, A. H., 2006b: The probability distribution of sea surface wind speeds. Part II: Dataset intercomparison and seasonal variability. *J. Climate*, **19**, 521-534.

Munday, D. R., H. L. Johnson, and D. P. Marshall, 2013: Eddy saturation of equilibrated circumpolar currents. *J. Phys. Oceanogr.*, **43**, 507-532.

Munday, D. R., and X. Zhai, 2015: Sensitivity of Southern Ocean circulation to wind stress changes: Role of relative wind stress, *Ocean Modell.*, **95**, 15-24.

Naström, G. D., K. S. Gage, and W. H. Jasperson R. M., 1984: Kinetic energy spectrum of large and mesoscale atmospheric processes, *Nature*, **310**, 36–38.

Ponte, R. M., and R. D. Rosen, 2004: Nonlinear effects of variable winds on ocean stress climatologies, *J. Climate*, **17**, 1283–1293.

Rayner, D. et al., 2011: Monitoring the Atlantic meridional overturning circulation. *Deep-Sea Res.*, **58**(17): 1744-1753.

Reynaud, T. H., A. J.Weaver, and R. J. Greatbatch, 1995: Summer mean circulation of the northwestern Atlantic Ocean. *J. Geophys. Res.*, **100**,779–816, doi:10.1029/94JC02561.

Scott, R. B., and Y. Xu, 2009: An update on the wind power input to the surface geostrophic flow of the World Ocean. *Deep-Sea Res.*, **56**, 295-304.

Smith, K. S., 2007: The geography of linear baroclinic instability in Earth's oceans. *J. Mar. Res.*, **65**(5), 655-683.

Stammer, D., 1998: On eddy characteristics, eddy transports, and mean flow properties. *J. Phys. Oceanogr.*, **28**, 727-739.

Stammer, D, K. Ueyoshi, A. Köhl, et al., 2004: Estimating air-sea fluxes of heat, freshwater, and momentum through global ocean data assimilation. *J. Geophys. Res*., **109**(C5), doi:10.1029/2003JC002082.

Straub, D. N., 1993: On the Transport and Angular Momentum Balance of Channel Models of the Antarctic Circumpolar Current. *J. Phys. Oceanogr.*, **23**, 776-782.

Thomas, M. D., A. M. De Boer, H. L. Johnson, and D. P. Stevens, 2014: Spatial and temporal scales of Sverdrup balance. *J. Phys. Oceanogr*. **44**, 2644-2660.

Thompson, K. R., R. F. Marsden, and D. G. Wright , 1983: Estimation of low-frequency wind stress fluctuations over the open ocean, *J. Phys. Oceanogr.*, **13**, 1003-1011.

Trenberth, K. E. and J. M. Caron, 2001: Estimates of Meridional Atmosphere and Ocean Heat Transports. *J. Climate*, **14**, 3433-3443.

von Storch, J. S., H. Sasaki, and J. Marotzke, 2007: Wind-generated power input to the deep ocean: An estimate using a 1/10 general circulation model. *J. Phys. Oceanogr.*, **37**,657-672.

Wang, Z., 2013: On the responses of Southern Hemisphere subpolar gyres to climate change in coupled climate models. *J. Geophys. Res*., **118**, 1070-1086, doi:10.1002/jgrc.20111.

Wang, Z., and M. P. Meredith, 2008: Density-driven Southern Hemisphere subpolar gyres in coupled climate models. *Geophys. Res. Lett*., **35**, L14608, doi:10.1029/2008GL034344.

Wang, Z., T. Kuhlbrodt, and M. P. Meredith, 2011: On the responses of the Antarctic Circumpolar Current transport to climate change in coupled climate models. *J. Geophys. Res*., **116,** C08011, doi:10.1029/2010JC006757.

Wilson, C., C. W. Hughes, and J. R. Blundell, 2015: Forced and intrinsic variability in the response to increased wind stress of an idealized Southern Ocean. *J. Geophys. Res*., **120**, 113-130.

Wunsch, C., 1998: The work done by the wind on the oceanic general circulation. *J. Phys. Oceanogr.*, **28**, 2332-2340.

Wunsch, C., 2011: The decadal mean ocean circulation and Sverdrup balance. *J. Mar. Res*., **69**, 417-434.

Wunsch, C., and R. Ferrari, 2004: Vertical mixing, energy, and the general circulation of the oceans, *Annu. Rev. Fluid Mech*., **36**, 281-314.

Wunsch, C., and P. Heimbach, 2013: Dynamically and kinematically consistent global ocean circulation state estimates with land and sea ice, in *Ocean Circulation and Climate: A 21st Century Perspective*, edited by G. Sielder et al., 2nd ed., 898 pp., Academic Press, Oxford, U.K.

Zhai, X., 2013: On the wind mechanical forcing of the ocean general circulation. *J. Geophys. Res*, **118**, 6561-6577, doi: 10.1002/2013JC009086.

Zhai, X., and D. P. Marshall, 2013: Vertical Eddy Energy Fluxes in the North Atlantic Subtropical and Subpolar Gyres. *J. Phys. Oceanogr.*, 43, 95-103.

Zhai, X., and C. Wunsch, 2013: On the Variability of Wind Power Input to the Oceans with a Focus on the Subpolar North Atlantic. *J. Climate*, **26**,3892-3903.

Zhai, X., H. L. Johnson, and D. P. Marshall, 2014: A Simple Model of the Response of the Atlantic to the North Atlantic Oscillation. *J. Climate*, **27**, 4052-4069.

Zhai, X., R. J. Greatbatch, C. Eden, and T. Hibiya, 2009: On the Loss of Wind-Induced Near-Inertial Energy to Turbulent Mixing in the Upper Ocean. *J. Phys. Oceanogr.*, **39**, 3040-3045.

Zhai, X., H. L. Johnson, D. P. Marshall, and C. Wunsch, 2012: On the wind power input to the ocean general circulation. *J. Phys. Oceanogr.*, **42**, 1357-1365.

List of Tables

TABLE 1. The mean strength of the main ocean gyres in Exp-6HR and Exp-MON (in Sv).

	North Atlantic Subpolar Gyre	North Atlantic Subtropical Gyre	South Atlantic Subtropical Gyre	North Pacific Subpolar Gyre	North Pacific Subtropical Gyre	South Pacific Subtropical Gyre	ACC
Exp-6HR	52.9	87.3	80.4	30.3	117.5	42.3	115.8
Exp-MON	36.3	80.2	70.1	15.5	100.3	35.7	111.5

List of Figures

1. The magnitude of time-mean surface wind stress (N m^{-2}) in (a) Exp-6HR, (b) Exp-MON, and (c) their difference (a-b).
2. Probability density distributions of (a) wind speed, (b) wind stress and (c) surface heat flux at low latitudes ([10^oN-20^oN, 75^oW-0^o]; dashed) and mid latitudes ([40^oN-60^oN, 75^oW-0^o]; solid) in Exp-6HR (black) and Exp-MON (red).
3. As in Fig.1, but for the time-mean wind stress curl (N m^{-3}). The black lines are contours of zero wind stress curl.
4. As in Fig. 1, but for the time-mean surface heat flux (W m^{-2}).
5. As in Fig. 1, but for the time-mean freshwater flux (kg m^{-2} s^{-1}).
6. As in Fig. 1, but for the time-mean wind power input to the ocean circulation (W m^{-2}).
7. Power input (W m^{-2}) to the surface geostrophic motions in (a) Exp-6HR and (b) Exp-MON. (c) is power input calculated using wind stress from Exp-MON and surface geostrophic currents from Exp-6HR.
8. As in Fig. 1, but for the time-mean surface EKE (m^2 s^{-2}).
9. As in Fig. 1, but for the time-mean barotropic streamfuncions (Sv).
10. (a) Time series of ACC transport (Sv) through Drake Passage and (b) zonally averaged density distribution (kg m^{-3}) in the Southern Ocean in Exp-6HR (black) and Exp-MON (red). In (b) a constant density of 1025 kg m^{-3} has been subtracted.

11. As in Fig. 1, but for the March-mean MLD in the Northern Hemisphere and September-mean MLD in the Southern Hemisphere (m).
12. Time series of the March-mean (a) MLD, (b) surface heat flux and (c) wind stress curl within the 3000-m isobath of the Labrador Sea.
13. As in Fig. 1, but for the time-mean AMOC (Sv).
14. Time series of the monthly AMOC (Sv) at 26.5^{o}N simulated in Exp-6HR (black) and Exp-MON (red) and that measured by the RAPID array (blue). The bold lines represent 12-month moving averages.
15. The time-mean meridional heat transport (PW) of (a) the global ocean, (b) the Atlantic Ocean, (c) the Pacific Ocean, and (d) the Indian Ocean in Exp-6HR (solid) and Exp-MON (dotted).

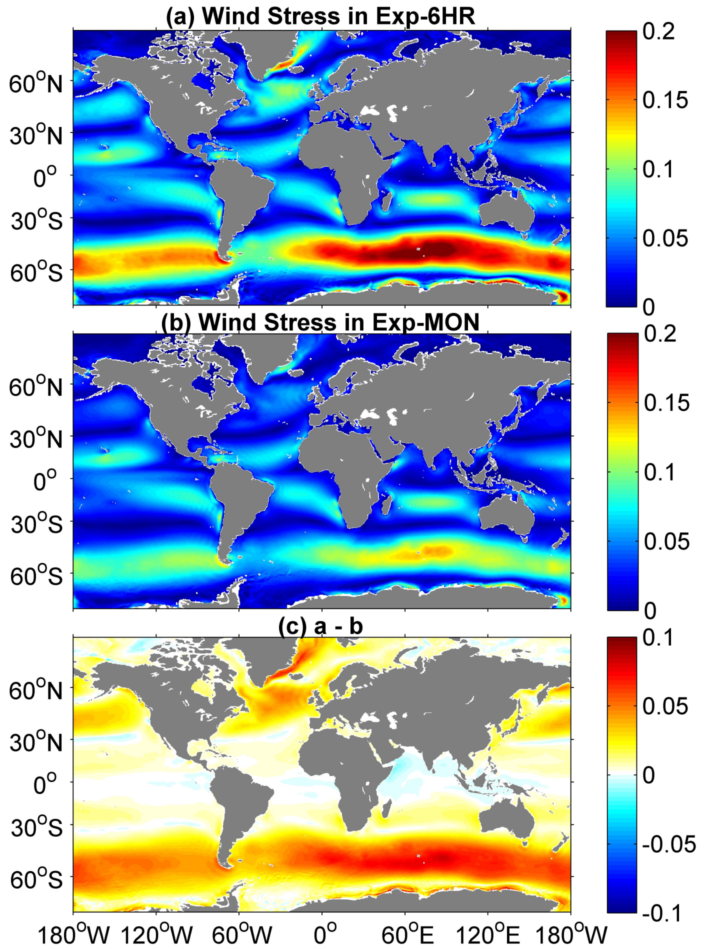

FIG. 1. The magnitude of time-mean surface wind stress (N m^{-2}) in (a) Exp-6HR, (b) Exp-MON, and (c) their difference (a-b).

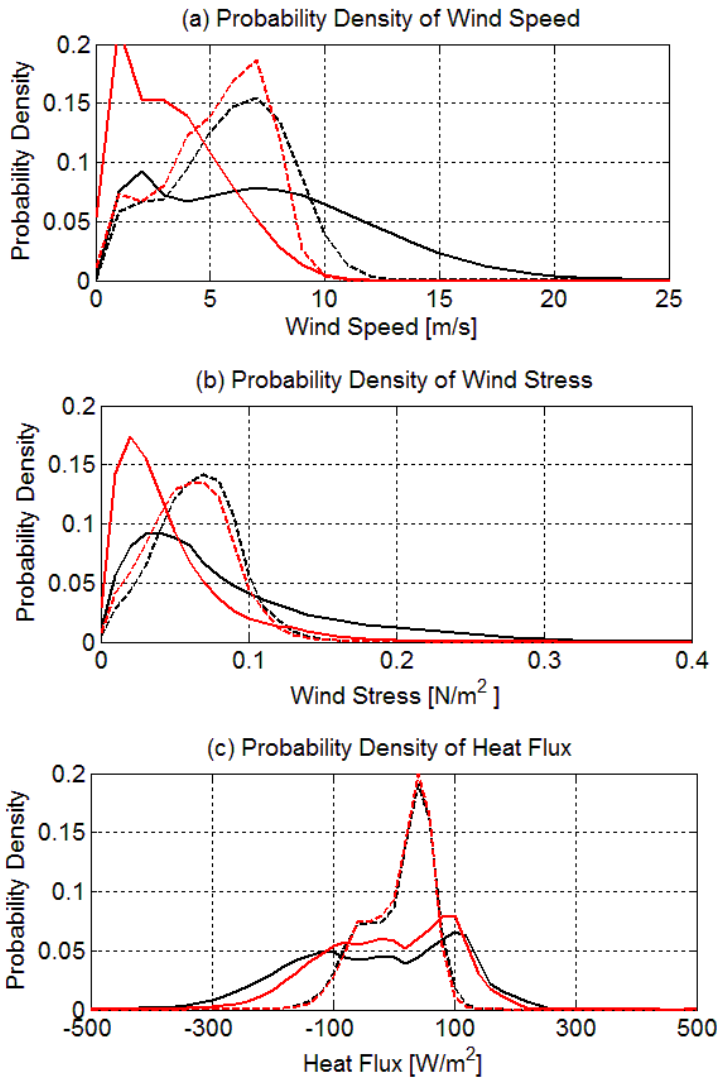

FIG. 2. Probability density distributions of (a) wind speed, (b) wind stress and (c) surface heat flux at low latitudes ([10°N-20°N, 75°W-0°]; dashed) and mid latitudes ([40°N-60°N, 75°W-0°]; solid) in Exp-6HR (black) and Exp-MON (red).

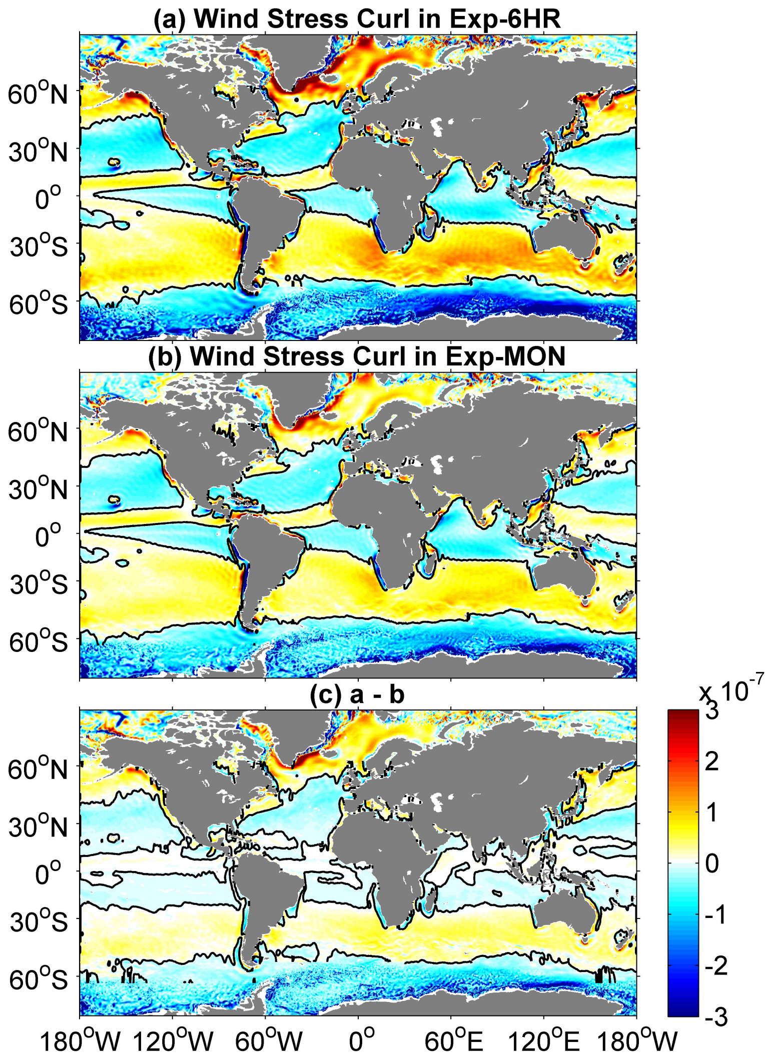

FIG. 3. As in Fig.1, but for the time-mean wind stress curl (N m^{-3}). The black lines are contours of zero wind stress curl.

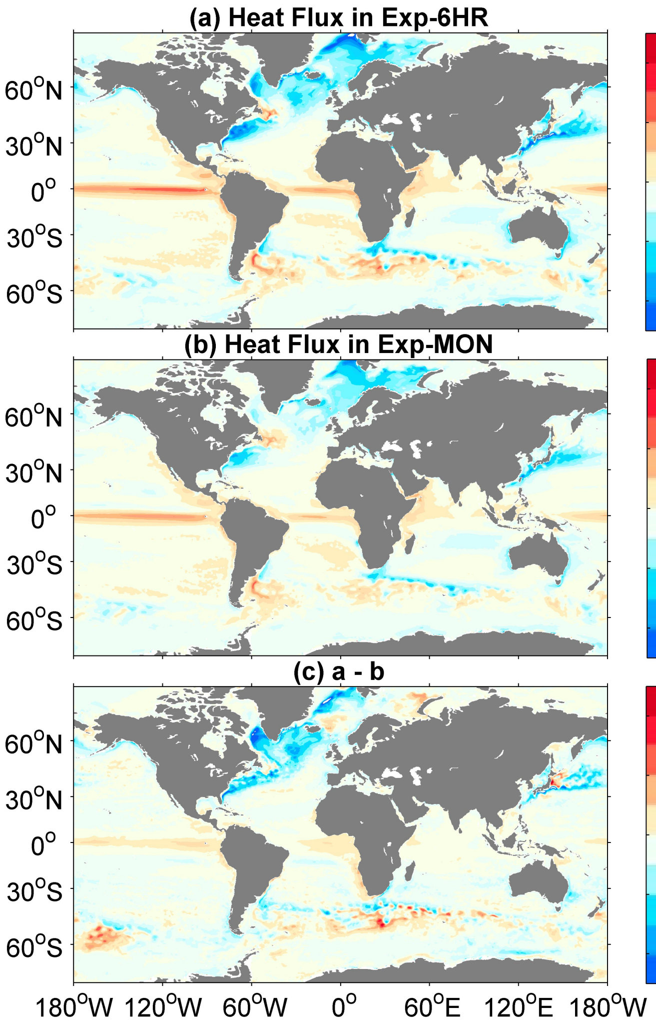

FIG. 4. As in Fig. 1, but for the time-mean surface heat flux (W m^{-2}).

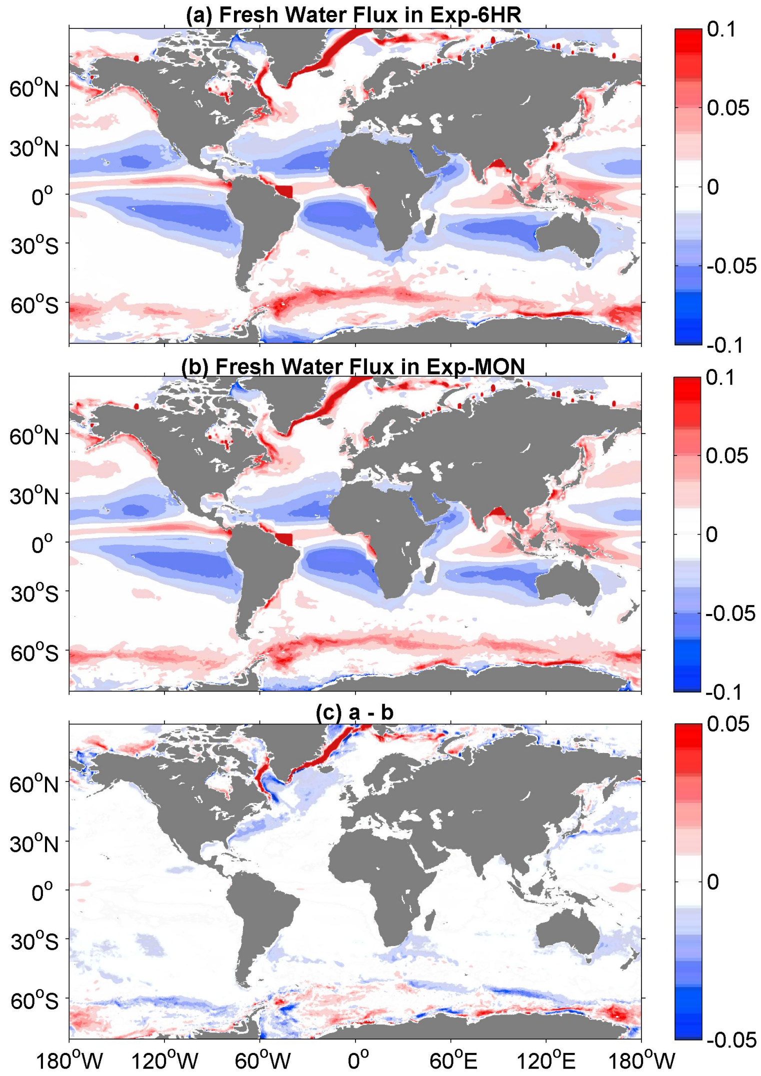

FIG. 5. As in Fig. 1, but for the time-mean freshwater flux (kg m^{-2} s^{-1}).

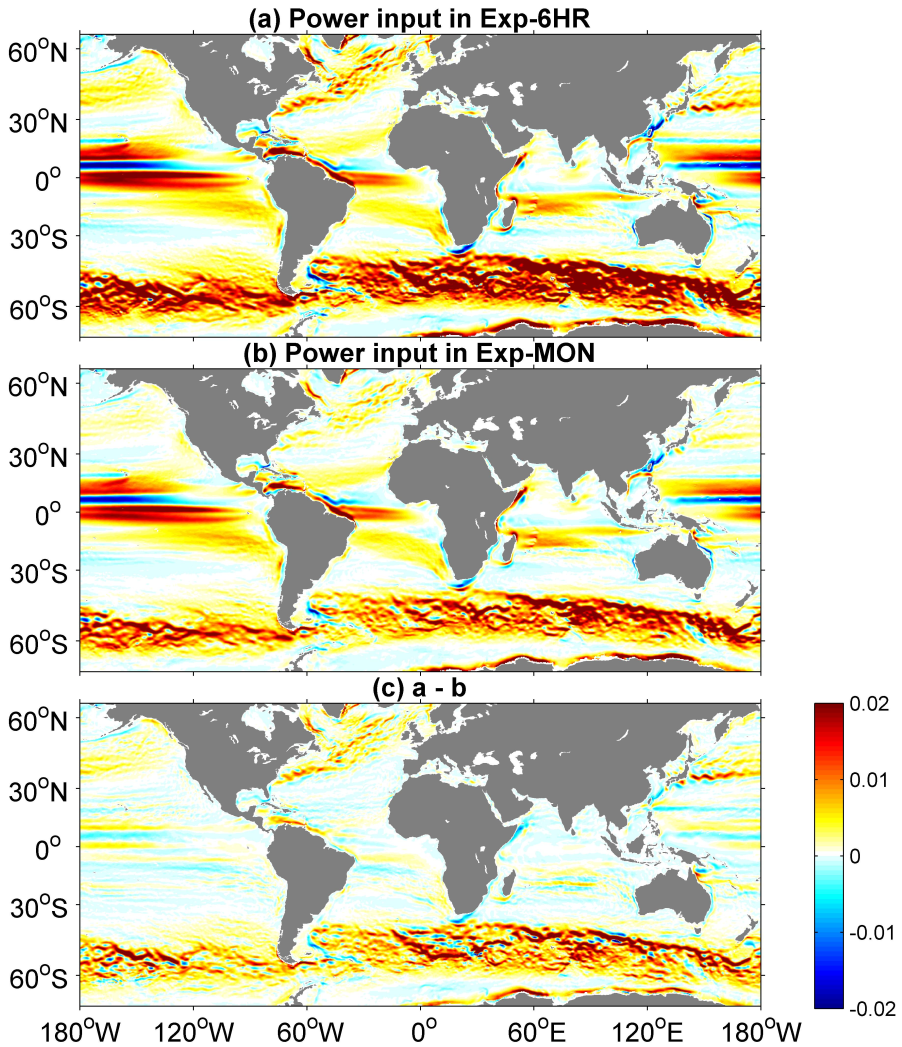

963

964

965 FIG. 6. As in Fig. 1, but for the time-mean wind power input to the ocean circulation

966 (W m^{-2}).

967

968

969

970

971

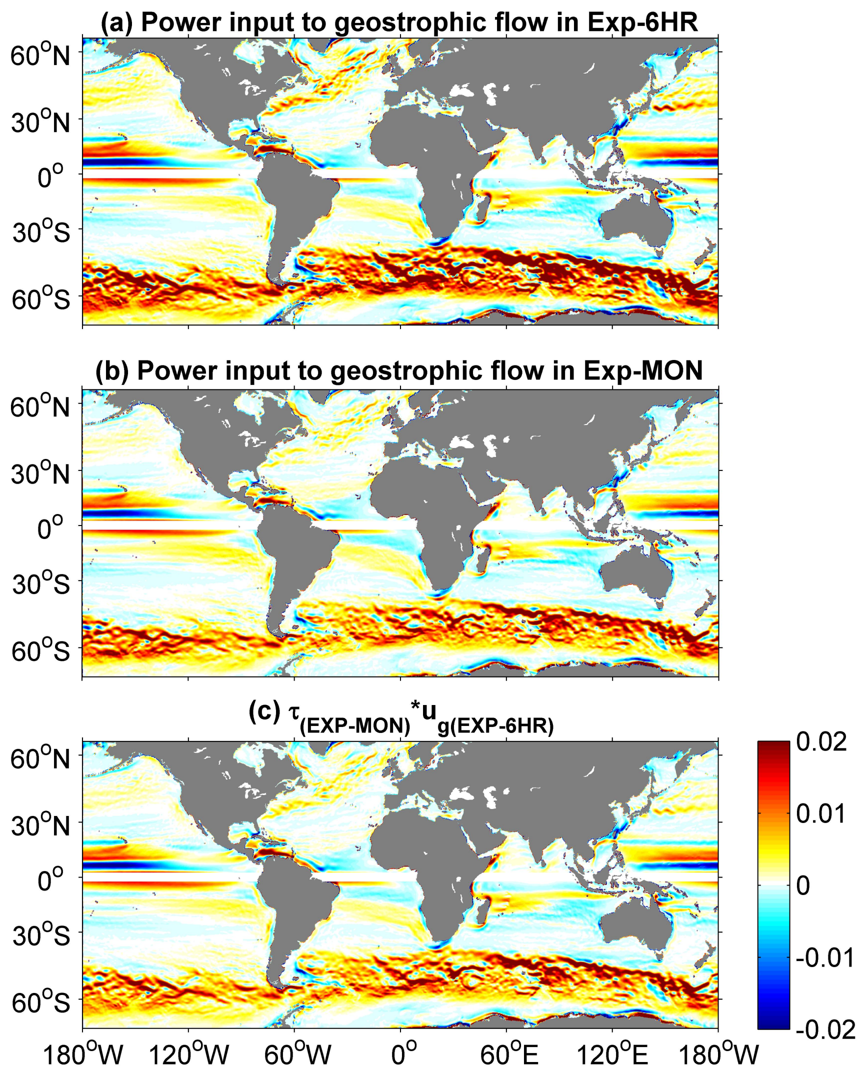

FIG. 7. Power input (W m^{-2}) to the surface geostrophic motions in (a) Exp-6HR and (b) Exp-MON. (c) is power input calculated using wind stress from Exp-MON and surface geostrophic currents from Exp-6HR.

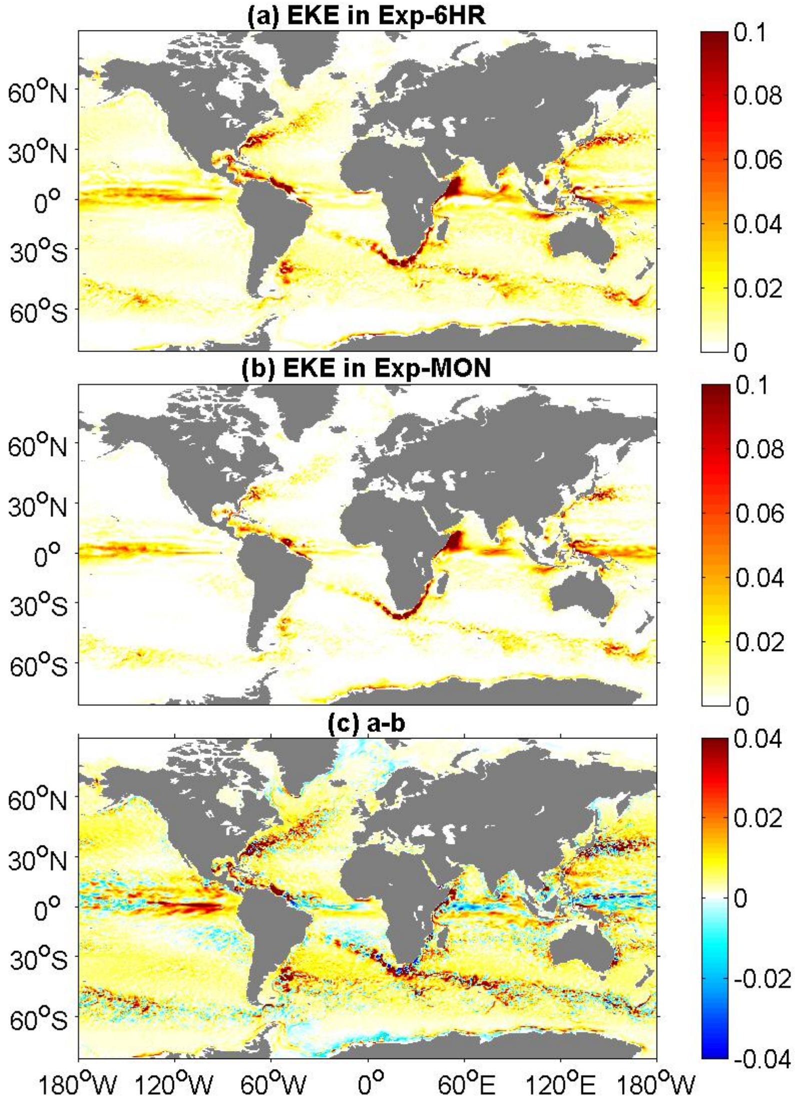

FIG. 8. As in Fig. 1, but for the time-mean surface EKE (m^2 s^{-2}).

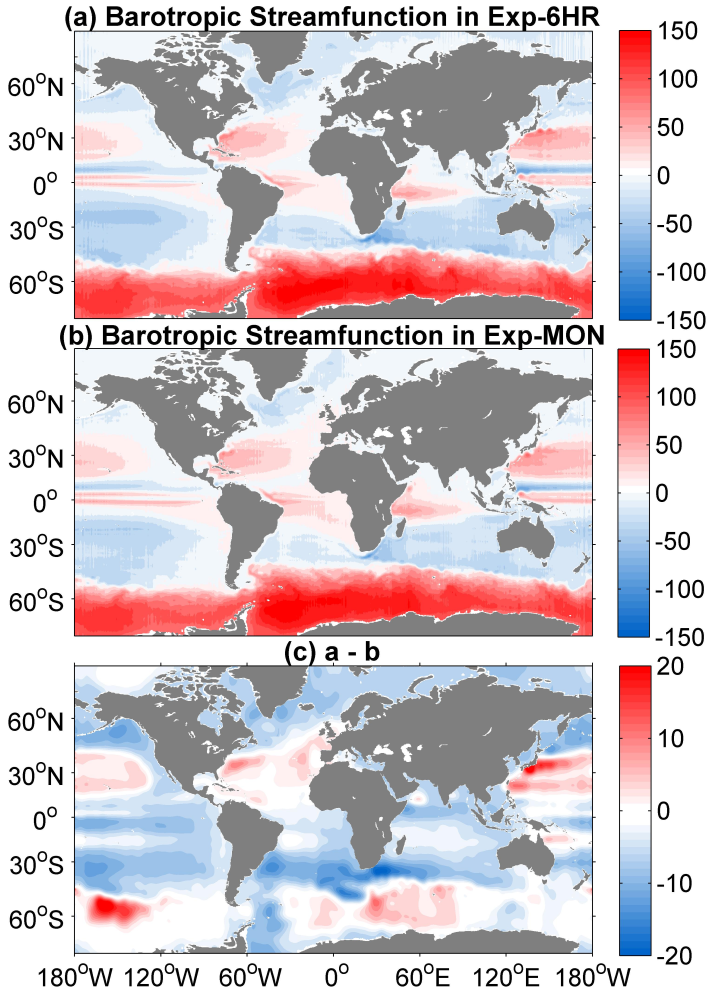

FIG. 9. As in Fig. 1, but for the time-mean barotropic streamfuncions (Sv).

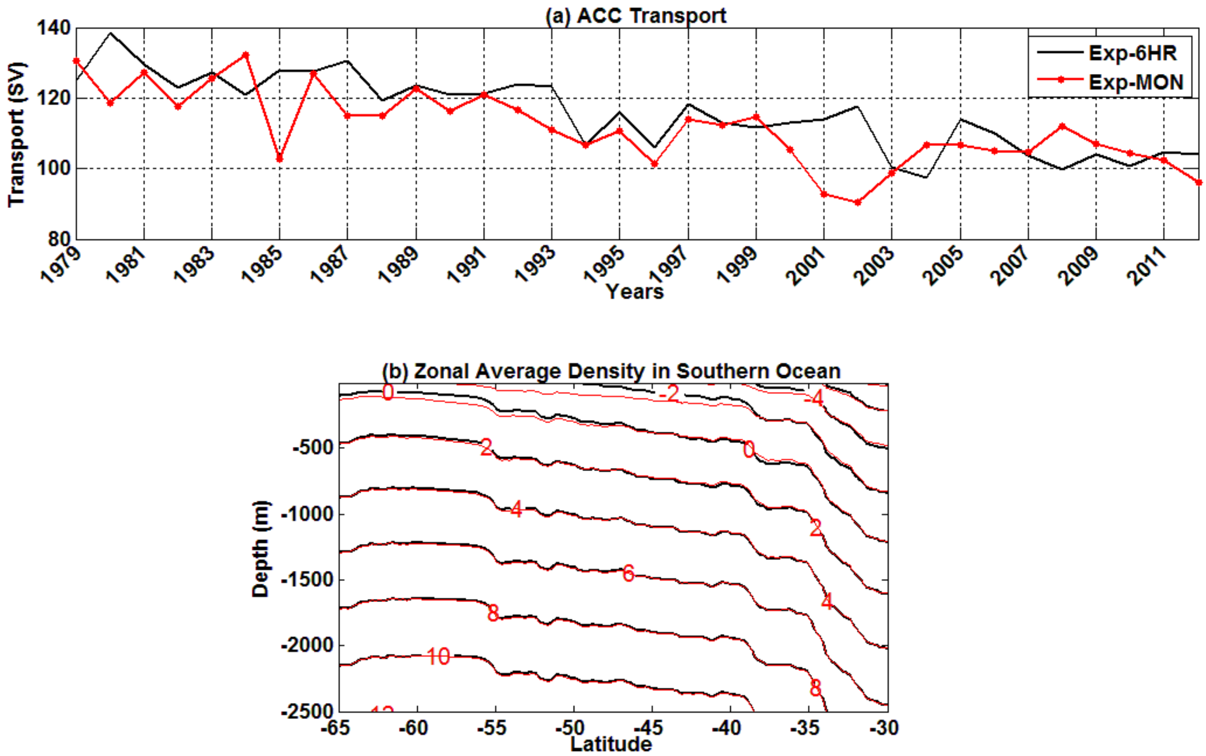

FIG. 10. (a) Time series of ACC transport (Sv) through Drake Passage and (b) zonally averaged density distribution (kg m^{-3}) in the Southern Ocean in Exp-6HR (black) and Exp-MON (red). In (b) a constant density of 1025 kg m^{-3} has been subtracted.

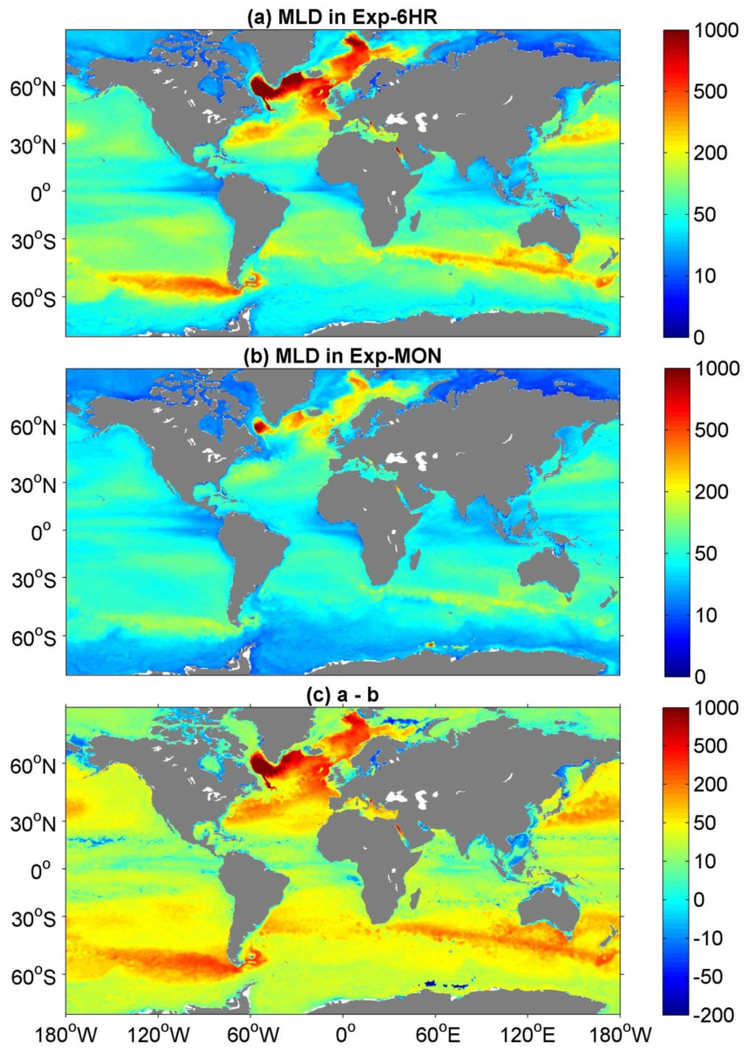

FIG. 11. As in Fig. 1, but for the March-mean MLD in the Northern Hemisphere and September-mean MLD in the Southern Hemisphere (m).

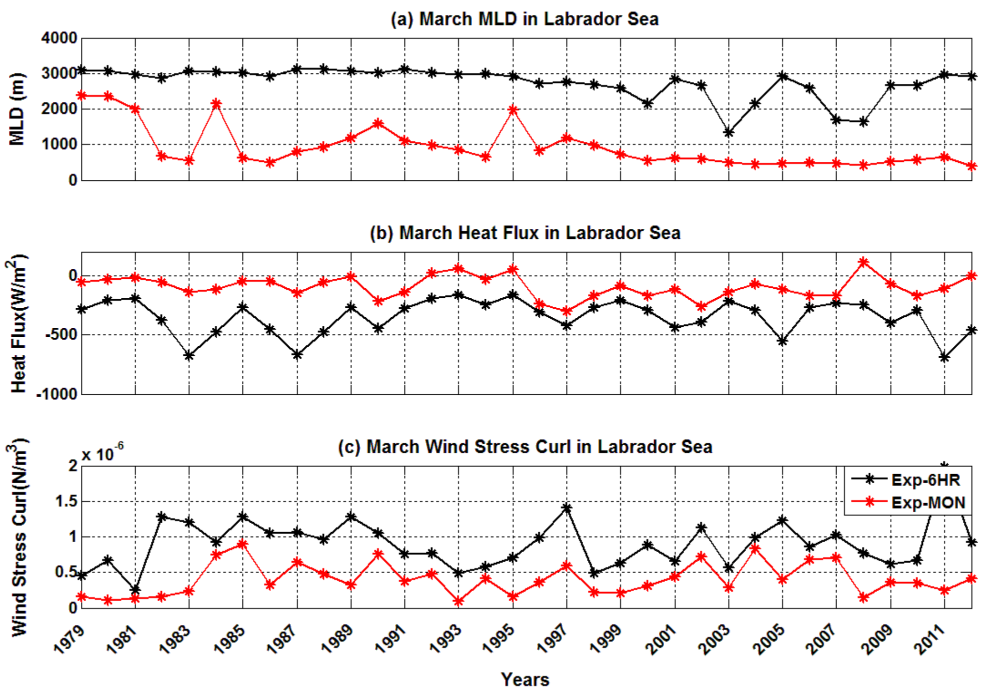

FIG. 12. Time series of the March-mean (a) MLD, (b) surface heat flux and (c) wind stress curl within the 3000-m isobath of the Labrador Sea.

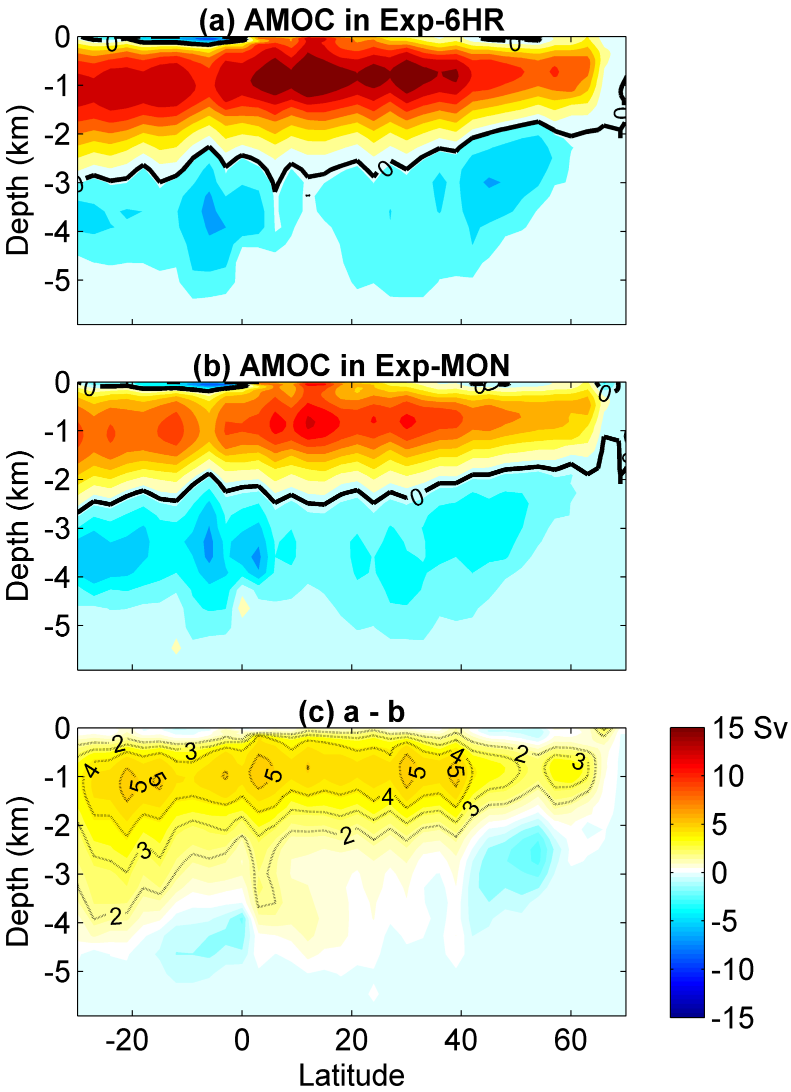

FIG. 13. As in Fig. 1, but for the time-mean AMOC (Sv).

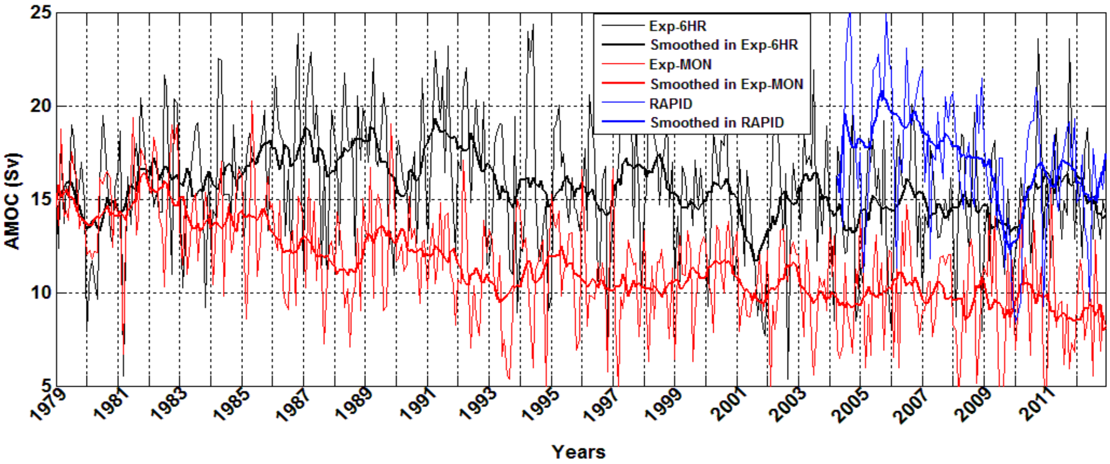

FIG. 14. Time series of the monthly AMOC (Sv) at 26.5^{o}N simulated in Exp-6HR (black) and Exp-MON (red) and that measured by the RAPID array (blue). The bold lines represent 12-month moving averages.

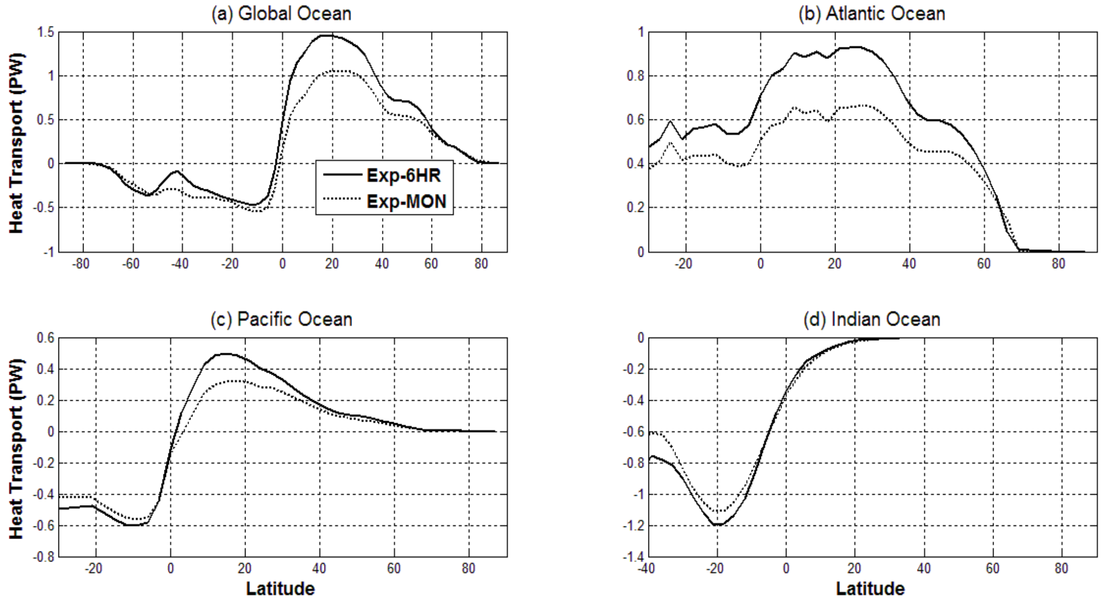

FIG. 15. The time-mean meridional heat transport (PW) of (a) the global ocean, (b) the Atlantic Ocean, (c) the Pacific Ocean, and (d) the Indian Ocean in Exp-6HR (solid) and Exp-MON (dotted).